



Star-shaped electron acceptors containing a truxene core for non-fullerene solar cells



Kaiwen Lin¹, Boming Xie¹, Zhenfeng Wang, Ruihao Xie, Yunping Huang, Chunhui Duan*, Fei Huang**, Yong Cao

Institute of Polymer Optoelectronic Materials and Devices, State Key Laboratory of Luminescent Materials and Devices, South China University of Technology, Guangzhou 510640, PR China

ARTICLE INFO

Keywords:

Truxene
Star-shaped molecules
Electron acceptors
Non-fullerene solar cells

ABSTRACT

A series of new electron acceptors containing a truxene core with intense optical absorption were synthesized and used for non-fullerene organic solar cells. Due to the weak electron-donating characteristic of truxene core and thereby weak intramolecular charge transfer interaction from electron-donating core to electron-withdrawing end groups, the resulting new acceptors show relatively wide optical band-gap and high-lying lowest unoccupied molecular orbitals (LUMOs), which consequently lead to complementary light spectra with narrow band-gap donor polymers and high open circuit voltage (V_{oc}) in solar cells. Particularly, **Tr(Hex)₆-3BR**, a star-shaped planar acceptor, produced the highest power conversion efficiency of 2.1% with a high V_{oc} of 1.02 V when blended with PTB7-Th.

1. Introduction

Over the past two decades, organic solar cells (OSCs) composed of electron donors and fullerene-based acceptors have attracted enormous attentions and made remarkable progress. The fullerene-based acceptors have high electron affinity and electron mobility, ensuring efficient exciton dissociation and charge transport. Therefore, high performance OSCs with power conversion efficiencies (PCEs) surpassed 11% have been achieved in fullerene-based devices [1,2]. However, fullerene-based acceptors suffer from a few drawbacks such as weak light absorption in the visible spectral region, limited variability in the energy levels, high cost of synthesis, and poor morphological stability in the blend films [3–6]. Recently, non-fullerene acceptors have made great achievements because of their tunable absorption spectra and energy levels, good chemical stability and photostability, as well as better compatibility with donors to form appropriate morphology [7–10]. Encouragingly, impressive PCEs over 13% have been realized by non-fullerene acceptors [11,12].

So far, state-of-the-art non-fullerene acceptors are based on linear acceptor-donor-acceptor (A-D-A) framework with planar conjugated backbone, which contain an electron-rich core and two electron-withdrawing terminal groups [5,6,9–16]. Among these successful materials, 3,9-bis(2-methylene-(3-(1,1-dicyano-methylene)-indanone))-5,5,11,11-

tetrakis(4-hexylphenyl)-dithieno[2,3-d:2',3'-d']-s-indaceno[1,2-b:5,6-b'] dithiophene (ITIC) [6], and (Z)-5-([5-(15-{(Z)-(3-Ethyl-4-oxo-2-thioxo-1,3-thiazolidin-5-ylidene)methyl]-8-thia-7.9-diazabicyclo [4.3.0]nona-1(9),2,4,6-tetraen-2-yl]-9,9,18,18-tetrakis(2-ethylhexyl)-5.14-dithiapentacyclo[10.6.0.0^{3,10}.0^{4,8}.0^{13,17}]octadeca-1(12),2,4(8),6,10,13(17),15-heptaen-6-yl)-8-thia-7.9-diazabicyclo [4.3.0]nona-1(9),2,4,6-tetraen-2-yl]methylidene)-3-ethyl-2-thioxo-1,3-thiazolidin-4-one (EH-IDTBR) [14–16] have shined in organic photovoltaics. Following this A-D-A strategy, we are interested in star-shaped planar acceptors rather than linear planar acceptors. Star-shaped molecules are capable of harvesting incident light efficiently owing to their extended dimensionality [17,18], which is beneficial to improving photocurrents in OSCs [19,20]. In addition, star-shaped molecules are able to achieve a proper balance between the size of molecular aggregation in solid state and exciton diffusion length scale to obtain good electronic communication due to moderate intermolecular interactions [20,21].

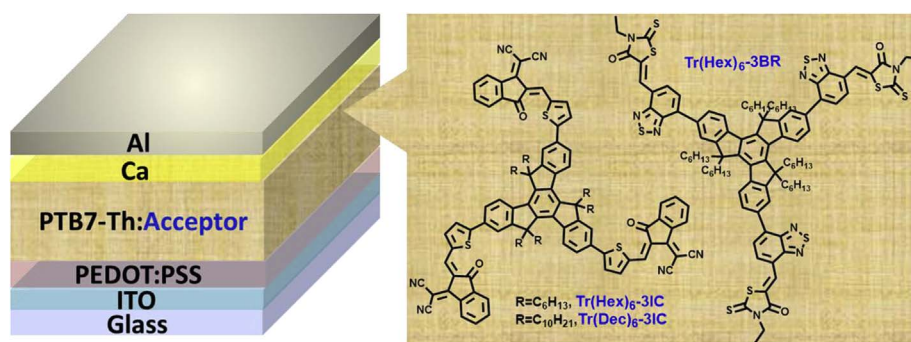
As an excellent building block for the construction of larger polyarenes, star-shaped molecule of truxene has been recognized and widely used in optoelectronic fields, such as dye-sensitized solar cells [22], perovskite solar cells [23,24], two-photon absorption materials [25], photocatalysts [26], organic light emitting diodes [27], and organic field effect transistors [28]. Moreover, truxene has been successfully

* Corresponding author.

** Corresponding author.

E-mail addresses: duanchunhui@scut.edu.cn (C. Duan), msfhuang@scut.edu.cn (F. Huang).

¹ These authors contributed equally to this work.



Scheme 1. Device structure employed in this study and the chemical structures of truxene-based acceptors.

employed in constructing electron donors for OSCs [29]. However, truxene has never been used to construct electron acceptors for OSCs. The truxene unit has rigid planar and C_{3h} symmetric structure. As a result, the resulting star-shaped acceptors will be capable of harvesting incident light efficiently due to the extended molecular dimensionality and well-delocalized conjugated structure [30]. Besides, the weak electron-donating characteristic of truxene core and thereby weak intramolecular charge transfer interaction from electron-donating core to electron-withdrawing end groups will endow the resulting new acceptors relatively wide optical band-gap and high-lying lowest unoccupied molecular orbitals (LUMOs), which consequently lead to complementary light spectra with narrow band-gap donor polymers and high open circuit voltage (V_{oc}) in OSCs [31–33].

Based on these considerations, herein we developed three new acceptors with a truxene core, namely **Tr(Hex)₆-3IC**, **Tr(Dec)₆-3IC**, and **Tr(Hex)₆-3BR** (Scheme 1). Among these molecules, **Tr(Hex)₆-3IC** and **Tr(Dec)₆-3IC** possess the same thiophene π -bridges and terminal electron-withdrawing units of (2-(3-oxo-2,3-dihydroinden-1-ylidene)malononitrile). Different side chain of hexyl and decyl were introduced onto these two materials because alkyl chain length is proven to be an important factor that determines device performance [34,35]. These two star-shaped materials can be regarded as analogues of ITIC, because they possess the same terminal acceptor units of (2-(3-oxo-2,3-dihydroinden-1-ylidene)malononitrile). **Tr(Hex)₆-3BR** possesses hexyl side chains and double electron withdrawing units of benzo[2,1,3]thiadiazole and 3-ethylrhodanine. This material is a star-shaped analogue of another famous acceptor of EH-IDTBR. Among the three new acceptors, **Tr(Hex)₆-3BR** displayed a maximum absorption coefficient as high as $2.9 \times 10^5 \text{ cm}^{-1}$ in film. When combined with the widely used narrow band-gap donor polymer of PTB7-Th, the resulting OSCs based on **Tr(Hex)₆-3BR** acceptor achieved a PCE of 2.1% with a high V_{oc} of 1.02 V. Moreover, the structure-property relationship with these truxene-based acceptors are discussed in detail in this contribution.

2. Experimental section

2.1. Materials and synthesis

All reagents were obtained from commercial sources and used without further purification, unless otherwise specified. Solvents were dried before use (tetrahydrofuran (THF) from sodium/benzophenone, toluene was washed with H_2SO_4 and then treated with CaCl_2 , and CH_3CN from CaH_2). Scheme 2 shows the synthetic routes of the truxene-based acceptors. The detailed synthesis procedures are described as following.

2.1.1. Compound 1

1-Indanone (20.0 g, 151 mmol) was dissolved in the mixture solution of acetic acid (120 mL) and concentrated hydrochloric acid (60 mL). The solution was heated to 120 °C and refluxed for 24 h. The hot mixture was poured into 1 L ice water, then sodium carbonate was added slowly with stirring for 1 h. The yellow precipitate was filtered,

and washed with water, acetone, and dichloromethane to give an off-white powder (11 g, 65%). $^1\text{H NMR}$ (500 MHz, CDCl_3) δ : 7.98 (d, 3H), 7.71 (d, 3H), 7.51 (t, 3H), 7.40 (t, 3H), 4.29 (s, 6H). $^{13}\text{C NMR}$ (125 MHz, CDCl_3) δ : 144.21, 142.13, 137.54, 135.71, 127.35, 126.73, 125.56, 122.31, 36.98.

2.1.2. Compound 2a

In a three-necked flask containing compound 1 (10 g, 29 mmol) under argon protection, anhydrous THF (200 mL) was added and the suspension was stirred at -78 °C. *n*-BuLi (115.2 mL, 2.5 M) was added dropwise and the mixture was kept at -78 °C for 2 h. 1-Bromohexene (48.2 g) was injected slowly. The mixture was allowed to warm to room temperature and stirred overnight. After that, the mixture was poured into 1 L saturated NH_4Cl aqueous solution to quench the excess *n*-BuLi. The water phase was extracted with ethyl acetate, and then the combined organic phase was dried over MgSO_4 . After the solvent was removed, the crude product was subjected to silica gel column with hexane as eluent to give an off-white powder 2a ($R = \text{C}_6\text{H}_{13}$, 22 g, 95%). It was used directly in the next step without characterization.

2.1.3. Compound 2b

Compound 2b was synthesized similarly to compound 2a with a yield of 92% by using 1-bromodecane to react with compound 1.

2.1.4. Compound 3a

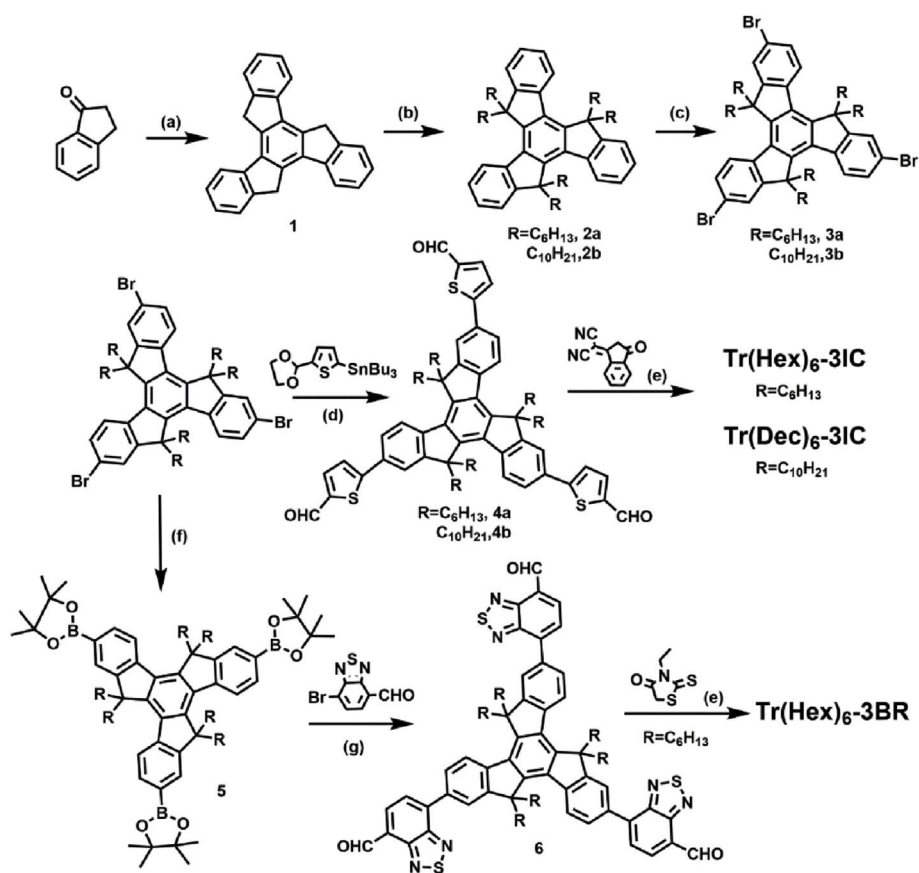
A mixture of compound 2a (2.4 g, 2.8 mmol), anhydrous FeCl_3 (5 mg) and chloroform (15 mL) was stirred. And then a solution of bromine (0.5 mL, 10 mmol) in 5 mL of chloroform was added dropwise under stirring at 0 °C, then kept overnight. Na_2SO_3 aqueous solution (50 mL) was added to remove excess bromine. The mixture was extracted with dichloromethane for three times, and the organic phase was dried over MgSO_4 . After the solvent was removed, the yellow residue was recrystallized from ethanol to yield an off-white powder (2.65 g, 89%). $^1\text{H NMR}$ (500 MHz, CDCl_3) δ : 8.18 (d, 3H), 7.56 (d, 3H), 7.52 (dd, 3H), 2.87 (dd, 6H), 2.04 (m, 6H), 0.93 (m, 36H), 0.63 (m, 18H), 0.46 (m, 14H). $^{13}\text{C NMR}$ (125 MHz, CDCl_3) δ : 156.02, 145.04, 139.00, 137.77, 129.51, 126.04, 125.66, 121.18, 56.13, 36.95, 31.59, 29.51, 24.02, 22.40, 14.01.

2.1.5. Compound 3b

Compound 3b was synthesized similarly to compound 3a from compound 2b. $^1\text{H NMR}$ (500 MHz, CDCl_3) δ : 8.17 (d, 3H), 7.72 (d, 3H), 7.56 (dd, 3H), 2.83 (m, 6H), 2.04 (m, 6H), 0.91 (m, 102H), 0.51 (m, 12H). $^{13}\text{C NMR}$ (125 MHz, CDCl_3) δ : 156.22, 145.11, 139.02, 137.55, 129.55, 126.24, 125.67, 121.28, 56.35, 36.98, 32.29, 29.99, 29.97, 29.80, 29.70, 29.61, 24.32, 23.10, 14.28.

2.1.6. Compound 4a

A mixture of compound 3a (0.615 g, 0.568 mmol), (5-(1,3-dioxolan-2-yl)thiophen-2-yl)trimethylstannane (1.136 g, 2.556 mmol), tetrakis (triphenylphosphine)palladium(0) (146 mg) were dissolved in toluene (70 mL) and degassed with argon for 30 min. The mixture was refluxed



Scheme 2. Synthetic routes of truxene-based acceptors. Reagents and conditions: (a) HCl, HOAc, 120 °C; (b) *n*-BuLi, THF, −78 °C; 1-bromohexene/1-bromodecane; (c) FeCl₃, CHCl₃, Br₂, 0 °C; (d) Pd(PPh₃)₄, toluene, 100 °C; (e) chloroform, pyridine, 65 °C; (f) bis(pinacolato)diboron, CH₃COOK, DMF, Pd(dppf)₂Cl₂, 90 °C; (g) toluene, Pd(PPh₃)₄, K₂CO₃, 95 °C.

for 48 h, then cooled to room temperature. HCl solution (1 M, 90 mL) was added into the mixture and stirred overnight. The mixture was extracted with dichloromethane, and the organic phase was dried over MgSO₄. After solvent evaporation the product was purified by flash column chromatography on silica gel (eluent, dichloromethane:petroleum ether = 1:1) to afford compound **4a** as a yellow solid (409 mg, 65%). ¹H NMR (500 MHz, CDCl₃) δ: 9.94 (s, 3H), 8.43 (d, 3H), 7.82 (d, 3H), 7.77 (d, 6H), 7.57 (d, 3H), 2.99 (m, 6H), 2.18 (m, 6H), 0.93 (m, 36H), 0.87 (m, 30H). ¹³C NMR (125 MHz, CDCl₃) δ: 155.34, 155.31, 146.98, 142.93, 142.07, 138.58, 138.24, 138.07, 125.88, 125.58, 124.70, 120.59, 56.71, 37.72, 32.13, 30.10, 24.67, 22.93, 14.55.

2.1.7. Compound 4b

Compound **4b** was synthesized similarly to compound **4a** from compound **3b**. ¹H NMR (500 MHz, CDCl₃) δ: 9.94 (s, 3H), 8.43 (d, 3H), 7.82 (d, 3H), 7.79 (d, 6H), 7.57 (d, 3H), 2.99 (m, 6H), 2.17 (m, 6H), 1.13 (m, 84H), 0.87 (m, 18H), 0.52 (m, 12H). ¹³C NMR (125 MHz, CDCl₃) δ: 155.05, 155.02, 146.67, 142.60, 141.81, 138.27, 137.90, 131.75, 125.59, 125.22, 124.33, 120.25, 56.38, 37.30, 32.26, 30.08, 29.97, 29.76, 29.67, 29.61, 24.36, 23.00, 14.42.

2.1.8. Compound 5

A mixture of compound **3a** (0.88 g, 0.82 mmol), bis(pinacolato)diboron (1.4 g, 5.5 mmol), CH₃COOK (0.61 g, 6.2 mmol), and *N,N*-dimethylformamide (30 mL) was carefully degassed before Pd(dppf)₂Cl₂ (50 mg, 0.082 mmol) was added. The mixture was stirred for 48 h at 90 °C under argon. Water and dichloromethane (300 mL) were added, and the organic layer was separated and washed with water three times. After removal of the solvent, the crude product was chromatographically purified on silica gel column (eluted with ethyl acetate:petroleum ether = 1:20) to afford compound **5** as a white solid (0.51 g, 51%). ¹H NMR (500 MHz, CDCl₃) δ: 8.39 (d, 3H), 7.87 (d, 3H),

7.85 (s, 3H), 2.95 (m, 6H), 2.16 (m, 6H), 1.42 (s, 36H), 0.89 (m, 36H), 0.59 (t, 18H), 0.45 (m, 12H). ¹³C NMR (125 MHz, CDCl₃) δ: 152.76, 146.45, 143.24, 138.33, 132.87, 128.21, 123.95, 83.73, 55.77, 36.84, 31.53, 29.52, 25.00, 23.97, 22.30, 13.89.

2.1.9. Compound 6

A mixture of compound **5** (0.613 g, 0.5 mmol) 2,1,3-benzothiadiazole-4-carboxaldehyde (0.546 g, 2.25 mmol) in anhydrous toluene (40 mL) was degassed for 30 min before Pd(PPh₃)₄ (58 mg, 0.05 mmol) and K₂CO₃ aqueous solution (2 M, 10 mL) was added. The solution was heated at 95 °C for 48 h. Water and dichloromethane were added, and the organic layer was dried over MgSO₄. After removal of the solvent, the crude product was chromatographically purified on silica gel column (eluted with ethyl acetate:petroleum ether = 1:20) to afford compound **6** as a yellow solid (0.46 g, 55%). ¹H NMR (500 MHz, CDCl₃) δ: 10.85 (s, 3H), 8.61 (d, 3H), 8.40 (d, 3H), 8.23 (d, 3H), 8.20 (d, 3H), 3.11 (m, 6H), 2.33 (m, 6H), 0.97 (m, 36H), 0.60 (m, 30H). ¹³C NMR (125 MHz, CDCl₃) δ: 189.44, 154.62, 154.50, 154.42, 147.28, 141.99, 140.89, 138.46, 134.97, 133.06, 128.38, 127.22, 126.59, 125.31, 124.02, 56.55, 37.46, 31.93, 29.94, 24.52, 22.72, 14.33.

2.1.10. Tr(Hex)₆-3IC

Compound **4** (0.15 g, 0.1275 mmol) and 2-(3-oxo-2,3-dihydroinden-1-ylidene)malononitrile (0.371 g, 3.825 mmol) were dissolved in chloroform (15 mL). A drop of pyridine was added and the solution was left to stir at 65 °C overnight. The reaction was dissolved in ethanol and stirred for another 10 min. The product was extracted with dichloromethane and dried over MgSO₄. After removal of the solvent, the crude product was chromatographically purified on silica gel column (eluted with chlorobenzene) to afford dark purple solid (105 mg, 85%). ¹H NMR (500 MHz, CDCl₃) δ: 8.95 (s, 3H), 8.75 (m, 3H), 8.50 (m, 3H), 8.01 (m, 3H), 7.98 (m, 6H), 7.91 (s, 3H), 7.83 (m, 6H), 7.69 (d, 3H), 3.04 (m, 6H), 2.28 (m, 6H), 0.95 (m, 36H), 0.62 (m, 30H). ¹³C NMR

(125 MHz, CDCl₃) δ : 187.44, 159.75, 159.54, 153.77, 145.88, 145.39, 141.05, 139.05, 137.13, 136.97, 135.96, 135.41, 134.29, 133.62, 130.51, 124.42, 124.40, 124.27, 123.99, 122.85, 121.62, 119.14, 113.53, 113.46, 70.06, 56.40, 37.23, 31.63, 29.57, 24.22, 22.41, 14.02. MS (MALDI-TOF) calculated for C₁₁₄H₁₀₈N₆O₃S₃, 1705.77; found, 1705.94.

2.1.11. Tr(Dec)₆-3IC

Tr(Dec)₆-3IC was synthesized similarly to **Tr(Hex)₆-3IC**. The product was obtained as a dark purple solid in 80% yield. ¹H NMR (500 MHz, CDCl₃) δ : 8.95 (s, 3H), 8.75 (m, 3H), 8.50 (d, 3H), 8.02 (m, 3H), 7.98 (m, 6H), 7.92 (d, 3H), 7.83 (m, 6H), 7.70 (d, 3H), 3.03 (m, 6H), 2.27 (m, 6H), 1.01 (m, 84H), 0.75 (m, 18H), 0.61 (m, 12H). ¹³C NMR (125 MHz, CDCl₃) δ : 187.42, 159.75, 159.56, 153.81, 145.92, 145.38, 141.08, 139.05, 137.11, 136.96, 135.97, 135.39, 134.28, 133.62, 130.49, 124.42, 124.34, 124.28, 123.92, 122.84, 121.59, 119.11, 113.54, 113.46, 70.28, 56.62, 37.35, 32.27, 30.10, 29.99, 29.79, 29.68, 29.67, 24.47, 23.00, 14.42. MS (MALDI-TOF) calculated for C₁₃₈H₁₅₆N₆O₃S₃, 2042.14; found, 2042.33.

2.1.12. Tr(Hex)₆-3BR

Tr(Hex)₆-3BR was synthesized similarly to **Tr(Hex)₆-3IC**. The product was obtained as a dark purple solid in 80% yield. ¹H NMR (500 MHz, CDCl₃) δ : 8.61 (m, 6H), 8.21 (m, 6H), 8.05 (d, 3H), 7.88 (d, 3H), 4.28 (m, 6H), 3.11 (m, 6H), 2.31 (m, 6H), 1.37 (m, 12H), 1.34 (m, 9H), 0.97 (m, 36H), 0.63 (m, 30H). ¹³C NMR (125 MHz, CDCl₃) δ : 193.04, 167.42, 154.60, 154.12, 153.40, 146.57, 141.18, 137.98, 136.48, 134.53, 131.03, 127.58, 127.43, 127.22, 125.51, 125.41, 124.79, 123.18, 56.01, 39.87, 36.99, 31.44, 29.46, 24.02, 22.22, 13.83, 12.24. MS (MALDI-TOF) calculated for C₉₉H₁₁₁N₉O₃S₉, 1762.63; found, 1763.76.

2.2. Instruments and characterization

¹H and ¹³C NMR spectra were tested on a Bruker AV-500 with tetramethylsilane (TMS) as an internal reference. MALDI-TOF-MS was performed by using a Bruker Agilent1290/maXis impact. UV-vis spectra were measured on a HP 8453 spectrophotometer. Thermogravimetric (TGA) analysis was measured on a NETZSCH TG 209 at a heating rate of 10 °C min⁻¹ with a nitrogen flow rate of 20 mL min⁻¹. Cyclic voltammetry data were measured on a CHI600D electrochemical workstation with Bu₄NPF₆ (0.1 M) in acetonitrile as the electrolyte, glass carbon electrode and a saturated calomel electrode as the working and reference electrodes, respectively. The thin films were coated on a glassy carbon working electrode. The scan rate was 100 mV s⁻¹. The onset potential of Fc/Fc⁺ was measured to be 0.36 V, and the HOMO and LUMO levels from the onset oxidation ($E_{\text{ox}}^{\text{onset}}$) and reduction ($E_{\text{red}}^{\text{onset}}$) potentials were calculated by equations: $E_{\text{HOMO}} = -e(E_{\text{ox}}^{\text{onset}} - E_{\text{Fc/Fc}^+} + 4.8)$ eV and $E_{\text{LUMO}} = -e(E_{\text{red}}^{\text{onset}} - E_{\text{Fc/Fc}^+} + 4.8)$ eV, respectively [36]. The geometry was optimized by Density Functional Theory (DFT) calculations performed at the B3LYP/6-31G(d) level to optimize the ground state geometries of the acceptor molecules using the Gaussian 09. The atom force microscopy (AFM) images were obtained from a NanoMan VS microscopy under tapping mode. The transmission electron microscopy (TEM) images were characterized with a JEM-2100F instrument.

2.3. Fabrication and characterization of solar cells

The device structure of ITO/PEDOT:PSS/PTB7-Th:acceptor/Ca/Al were fabricated as the following procedure. The ITO-coated glass substrate was cleaned in an ultrasonic bath with deionized water, acetone, and isopropanol, each process was approximately 15 min, and then dried under a stream of dry nitrogen. PEDOT:PSS (Heraeus Clevis P VP A 4083) was spin-coated on top of the above ITO and annealed in air at 150 °C for 10 min. Subsequently, the blend solutions of PTB7-Th and

acceptors were prepared by simultaneously dissolving both materials with weight ratio of 1:1 in chloroform and spin-coated on the ITO/PEDOT:PSS electrode (at 1600 rpm for 60 s) to form active layer with thickness of 100 nm. Then a 10 nm Ca and a 100 nm Al layer were thermally deposited onto the active layer through a shadow mask at a vacuum of 5×10^{-5} Pa. During the test, an aperture with an area of 3.14 mm² was used. The current density–voltage (J – V) curves were measured using AM1.5G solar simulator (Class AAA solar simulator, Model 94063A, Oriel) with an irradiation light intensity of 100 mW cm⁻². The external quantum efficiency (EQE) spectra were determined from a QEX10 Solar Cell IPCE measurement system (PV measurement, Inc).

2.4. Fabrication and characterization of single-carrier devices

The charge carrier mobilities of PTB7-Th:truxene-based acceptor blend films were determined from single-carrier devices with space-charge-limited current (SCLC) model. The device structures of the electron only and hole only devices are Al/PTB7-Th:truxene-based acceptor/Ca/Al and ITO/PEDOT:PSS/PTB7-Th:truxene-based acceptor/MoO₃/Ag, respectively. The mobilities were determined by fitting the dark J – V current to the model of a single carrier SCLC using the equation: $J = 9\epsilon_0\epsilon_r\mu V^2/8d^3$ [37], where J is the current density, d is the thickness of the blend films, ϵ_0 is the permittivity of free space, ϵ_r is the relative dielectric constant of the transport medium, and μ is the charge carrier mobility. $V = V_{\text{app}} - V_{\text{bi}}$, where V_{app} is the applied voltage and V_{bi} is the offset voltage. The carrier mobility can be calculated from the slope of the $J^{1/2}$ – V curves.

3. Results and discussion

3.1. Synthesis and characterization

Scheme 2 shows the synthetic routes of the truxene-based acceptors. The synthetic routes include cyclization of 1-indanone to produce truxene (compound **1**) [27–31,34,35], lithium-hydrogen exchange reaction to obtain alkyl chain modified truxene (compound **2**) [29,34], bromization reaction to yield compound **3** [29], Pd-catalyzed Stille cross-coupling to introduce π -bridge of thiophene, Pd-catalyzed Suzuki cross-coupling to introduce benzothiadiazole, and Knoevenagel condensation between terminal acceptor groups and truxene-based aldehydes to produce the target acceptor materials [11–15]. The purity of the final compounds were characterized by ¹H-, ¹³C-NMR spectroscopy, and MALDI-TOF MS, which indicates the high purity of these compounds (**Figs. S13–S21**, Supporting Information). All these acceptors are readily soluble in common organic solvents at room temperature, such as dichloromethane, and chloroform, which ensures the preparation of smooth and uniform films. The thermal stability of the acceptors was investigated by TGA under a nitrogen atmosphere. All materials show good thermal stability with 5% decomposition temperature (at 5% weight-loss) (T_d) over 350 °C (**Fig. S22**, Supporting Information). Among them, **Tr(Hex)₆-3BR** shows the best thermal stability with T_d above 400 °C.

3.2. Theoretical calculations

Density functional theoretical (DFT) calculations were performed at B3LYP/6-31G(d) level to study the molecular geometries and electron structures of the acceptors. To simplify the calculation, hexyl and decyl chains were replaced with methyl unit and the model structures were named as **Tr-3IC** and **Tr-3BR**. As shown in **Fig. 1**, the optimized molecular geometry reveals a quite planar structure for the star-shaped **Tr-3BR** with minimal torsion of the backbone. This highly planar geometry would facilitate π -electron delocalization and enhance charge transport property [11,12]. **Tr-3IC** is slight twisted with dihedral angles of 22.53° between truxene and thiophene units, 0.80° between

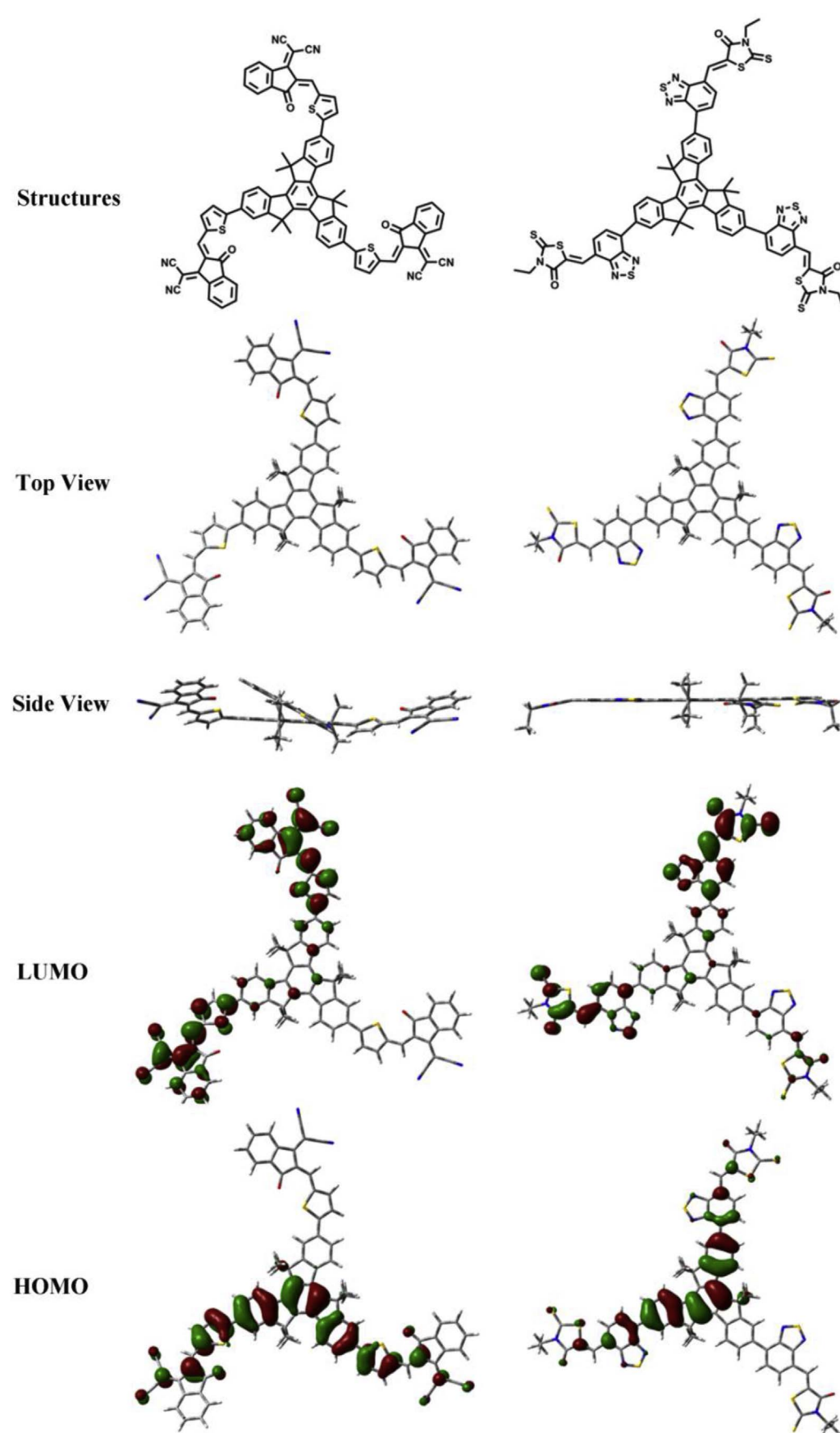


Fig. 1. DFT calculated molecular geometries and frontier molecular orbital distributions for the model structures (Tr-3IC and Tr-3BR).

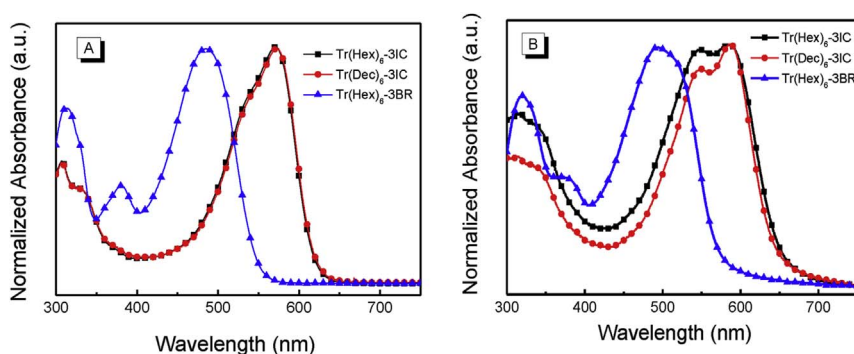


Fig. 2. Normalized absorption spectra of truxene-based acceptors in chloroform solutions (A) and as thin films (B).

thiophene and the terminal electron-withdrawing units. The distorted configuration may help to reduce intermolecular interactions and restrict the excessive self-aggregation and large-scale phase separation in the blend films [38]. To further study the alkyl chain effect on dihedral angles, **Tr(Hex)₆-3IC** and **Tr(Dec)₆-3IC** were calculated separately (Fig. S23, Supporting Information). The dihedral angles are not changed along with alkyl chain changes. The frontier molecular orbital distributions for the model structures were also calculated. The highest occupied molecular orbitals (HOMOs) are mainly distributed on the truxene core and the adjacent π -bridge, while the LUMOs are localized on the terminal units and benzothiadiazole unit due to their strong electron-withdrawing effect. It is expected that this large electron-accepting area will benefit charge transfer. The theoretical HOMO/LUMO energy levels of **Tr-3IC** and **Tr-3BR** are predicted to be $-5.87/-3.27$ and $-5.74/-2.94$ eV, respectively.

3.3. Optical and electrochemical properties

The UV–vis absorption spectra of the acceptors in solution and as thin film are displayed in Fig. 2. All acceptors show intense absorption in the range of 400–650 nm that can be ascribed to the intramolecular charge transfer (ICT) transitions between central truxene and terminal acceptor units [39,40]. In solutions, the absorption coefficients of all acceptors exceed $106 \text{ L g}^{-1} \text{ cm}^{-1}$ ($1.8 \times 10^5 \text{ M}^{-1} \text{ cm}^{-1}$). In particular, **Tr(Hex)₆-3BR** exhibits a maximum absorption coefficient as high as $165 \text{ L g}^{-1} \text{ cm}^{-1}$ ($2.9 \times 10^5 \text{ M}^{-1} \text{ cm}^{-1}$) at 482 nm (Fig. S24A, Supporting Information). The high absorption coefficients of these molecules are possibly owing to their extended dimensionality, which is consistent with other star-shaped molecules based on triphenylamine, triazatruxene, and benzotrithiophene that presented high molecular absorption coefficients over $1.0 \times 10^5 \text{ M}^{-1} \text{ cm}^{-1}$ [17,19,20]. The absorption bands of the truxene-based acceptors in film (Fig. 2B) are significantly red-shifted and broadened compared to that in chloroform solution, which can be attributed to the aggregation of the molecules in solid state [10,11]. Interestingly, the changes in the alkyl chain length on truxene lead to considerable spectral shifts. In solution, **Tr(Hex)₆-3IC** shows significantly red-shifted absorption relative to **Tr(Dec)₆-3IC**. In film, this difference becomes less considerable but **Tr(Hex)₆-3IC** still exhibits slightly wider ICT bands than **Tr(Dec)₆-3IC**. Encouragingly, **Tr(Hex)₆-3BR** displays a maximum absorption coefficient as high as $2.9 \times 10^5 \text{ cm}^{-1}$ in film (Fig. S24B, Supporting Information). The optical band gaps (E_g) of the acceptors are calculated to be 1.90 eV for **Tr(Hex)₆-3IC**, 1.92 eV for **Tr(Dec)₆-3IC**, and 2.15 eV for **Tr(Hex)₆-3BR**, respectively (Table 1).

The energy levels of truxene-based acceptors were determined by cyclic voltammetry (CV) (Fig. 3). The relevant data are summarized in Table 1. The HOMO/LUMO levels of **Tr(Hex)₆-3IC**, **Tr(Dec)₆-3IC**, and **Tr(Hex)₆-3BR** are $-5.92/-3.94$, $-5.88/-3.90$, and $-5.79/-3.74$ eV, respectively. The electrochemical band gaps (E_g^{CV}) are thus calculated to be 1.98, 1.98, and 2.05 eV, respectively. The higher LUMO level of **Tr(Hex)₆-3BR** compared to **Tr(Hex)₆-3IC** and **Tr(Dec)₆-3IC** may result in

a higher V_{oc} , due to V_{oc} is proportional to the offset between the LUMO level of the acceptor and the HOMO level of the donor [41].

3.4. Photovoltaic properties

The photovoltaic properties of the truxene-based acceptors were evaluated in OSCs with a structure of ITO/PEDOT:PSS/PTB7-Th:acceptor/Ca/Al (Scheme 1). PTB7-Th was used as the donor because its strong optical absorption at long-wavelength region can achieve complementary absorption with our truxene-based acceptors. The photoactive layers were formed by spin-coating the blend solutions of PTB7-Th:truxene-based acceptors (1:1, w/w) in chloroform without additives and post-processing. The optimum thickness of the photoactive layer is 100 nm (Table S1, Supporting Information). Fig. 4A shows the current density-voltage (J - V) curves and Table 2 lists the corresponding photovoltaic parameters. The acceptors produce a high V_{oc} in the range from 0.74 to 1.0 V. However, the acceptors can only afford moderate PCEs due to the relatively low short circuit current (J_{sc}) and fill factor (FF). **Tr(Hex)₆-3BR**-based devices offer the maximum PCE of 2.10% with a J_{sc} of 5.92 mA cm^{-2} , a high V_{oc} of 1.02 V and an FF of 33.4%. The high V_{oc} can be ascribed to the high LUMO energy level of **Tr(Hex)₆-3BR** [41]. The change of alkyl chains from hexyl (**Tr(Hex)₆-3IC**) to decyl (**Tr(Dec)₆-3IC**) is detrimental to device performance. The **Tr(Hex)₆-3IC**- and **Tr(Dec)₆-3IC**-based solar cells show the maximum PCE of 1.28% and 0.55%, respectively. Obviously, the photovoltaic parameters of **Tr(Hex)₆-3IC**- and **Tr(Dec)₆-3IC**-based solar cells are lower than other reported (2-(3-oxo-2,3-dihydroinden-1-ylidene)malononitrile end-capped electron acceptors [42–44]. Processing additives such as 1,8-diiodooctane (DIO) and 1-chloronaphthalene (CN) have been widely used for non-fullerene-based OSCs to improve PCEs [10–15]. However, DIO is not able to improve the performance of **Tr(Hex)₆-3BR** based devices (Table S2, Supporting Information).

Fig. 4B shows the corresponding external quantum efficiency (EQE) spectra of the solar cells based on **Tr(Hex)₆-3IC**, **Tr(Dec)₆-3IC**, and **Tr(Hex)₆-3BR**. For each device, the integration from the EQE curve matches well with the J_{sc} value acquired from the J - V curves. The **Tr(Hex)₆-3IC**- and **Tr(Dec)₆-3IC**-based devices exhibit a maximum EQE of 22% and 15% at 595 nm, and showed similar profile. The **Tr(Hex)₆-3BR**-based devices exhibit an EQE exceeding 20% in the range from 340 to 730 nm with the maximum value reaching 31% at around 505 nm. The broad EQE of **Tr(Hex)₆-3BR** devices indicate the efficient electron transfer from PTB7-Th to **Tr(Hex)₆-3BR** and efficient hole transfer from **Tr(Hex)₆-3BR** to PTB7-Th, which is beneficial to generating a higher PCE in devices [45].

The charge recombination of the devices were studied by measuring the photocurrent as a function of light intensity (from 1 to 100 mW cm^{-2}). The relevant characteristics are plotted in Fig. S25 (Supporting Information). Generally, J_{sc} and the intensity of incident light (P_{light}) follow the relationship of $J_{\text{sc}} \propto P_{\text{light}}^\alpha$, where the power-law component (α) will be unity when there is no bimolecular recombination [9,14]. The α values are 0.898 for **Tr(Hex)₆-3IC**, 0.828 for **Tr**

Table 1
Optical and electrochemical properties of truxene-based acceptors.

Acceptors	$\lambda_{\text{max}}^{\text{sol}}$ (nm)	$\lambda_{\text{max}}^{\text{film}}$ (nm)	E_g^{opta} (eV)	$E_{\text{ox}}^{\text{onset}}$ (V)	$E_{\text{red}}^{\text{onset}}$ (V)	$E_{\text{HOMO}}^{\text{b}}$ (eV)	$E_{\text{LUMO}}^{\text{c}}$ (eV)	E_g^{cvd} (eV)
Tr(Hex) ₆ -3IC	570	588	1.90	1.48	-0.50	-5.92	-3.94	1.98
Tr(Dec) ₆ -3IC	570	588	1.92	1.44	-0.54	-5.88	-3.90	1.98
Tr(Hex) ₆ -3BR	482	491	2.15	1.35	-0.70	-5.79	-3.74	2.05

^a Calculated from $E_g^{\text{opt}} = 1240/\lambda_{\text{onset}}^{\text{film}}$ eV.

^b Calculated from $E_{\text{HOMO}} = -e(E_{\text{ox}}^{\text{onset}} - E_{\text{Fc}/\text{Fc}^+} + 4.8)$ eV.

^c Calculated from $E_{\text{LUMO}} = -e(E_{\text{red}}^{\text{onset}} - E_{\text{Fc}/\text{Fc}^+} + 4.8)$ eV; ^d Calculated from $E_g^{\text{cv}} = E_{\text{LUMO}} - E_{\text{HOMO}}$.

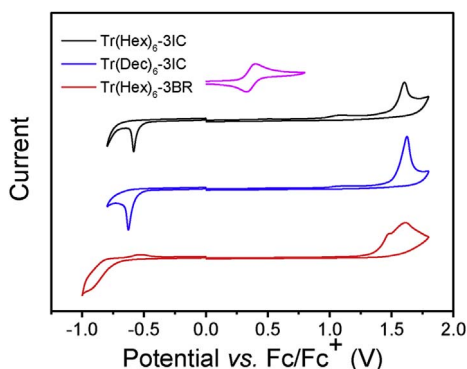


Fig. 3. Cyclic voltammograms of truxene-based acceptors in thin film.

(Dec)₆-3IC, and 0.858 for Tr(Hex)₆-3BR, respectively, which indicates considerable bimolecular recombination losses. Typically, charge recombination is related to the FF of the devices. The lower bimolecular recombination in the Tr(Hex)₆-3IC-based OSCs ($\alpha = 0.898$) agrees well with the higher FF value of the devices (38.1%) as compared to the other devices.

3.5. Charge carrier mobility

The charge transport properties of the blend films were investigated by fabricating single-carrier devices with a device structure of ITO/PEDOT:PSS/PTB7-Th:acceptor/MoO₃/Ag and Al/PTB7-Th:acceptor/Ca/Al for hole only devices and electron only devices, respectively. The hole and electron mobilities were acquired by fitting the J - V with space-charge-limited current (SCLC) model. The J - V curves of the devices are shown in Fig. 5. The hole mobilities (μ_{h}) are estimated to be 1×10^{-3} to 6×10^{-3} cm² V⁻¹ s⁻¹, which are comparable with the value that obtained from PTB7-Th:fullerene devices [46]. In contrast, the electron mobilities (μ_{e}) of the blend films of PTB7-Th:truxene-based acceptor are measured to be 1.5×10^{-5} to 2.0×10^{-6} cm² V⁻¹ s⁻¹, which are two or three orders of magnitude lower than that of PTB7-Th:fullerene film [47]. The low electron mobility and highly imbalanced $\mu_{\text{h}}/\mu_{\text{e}}$ seriously restrict the charge transport and result in bimolecular recombination, which in turn led to low FF and J_{sc} [8,48].

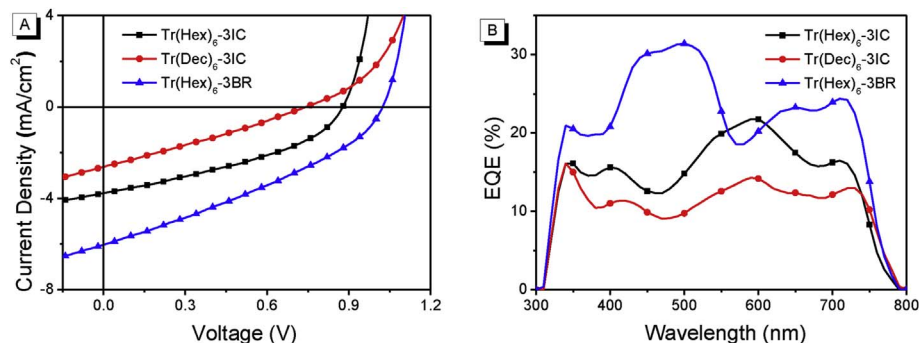


Fig. 4. J - V characteristics curves (A) and EQE spectra (B) of OSCs based on PTB7-Th and truxene-based acceptors.

This should be the main reason of low performance of these truxene-based acceptors. Among the three acceptors, Tr(Hex)₆-3BR exhibits the highest electron mobility in blend film, which may be attributable to its good planarity and favorable π - π stacking. As a result, Tr(Hex)₆-3BR-based devices achieve the highest J_{sc} , FF, and PCE (Table S3, Supporting Information).

3.6. Morphology

Atomic force microscopy (AFM) was used to investigate the morphology of blend films of PTB7-Th:truxene-based acceptor (Fig. 6). All the films were prepared on top of PEDOT:PSS using the same fabrication conditions for solar cells. The film of PTB7-Th:Tr(Hex)₆-3IC exhibits obvious phase separation with large granulate features, resulting in a relative coarse surface with a root-mean-square (RMS) surface roughness of 8.0 nm. It is well recognized that excessive aggregation and phase separation are detrimental to exciton dissociation [49]. The blends based on Tr(Dec)₆-3IC and Tr(Hex)₆-3BR show homogeneous films with a RMS roughness of 0.76 and 0.96 nm, respectively, indicating intimately mixed blends without noteworthy phase separation. With such a morphology, charge generation is impeded because of the lack of pure domains. High domain purity is favorable for dissociating photo-generated charges from the donor/acceptor interface, while low domain purity often causes serious geminate recombination.

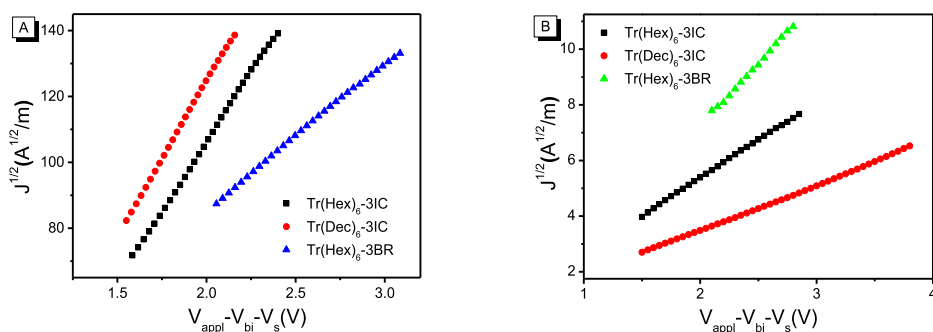
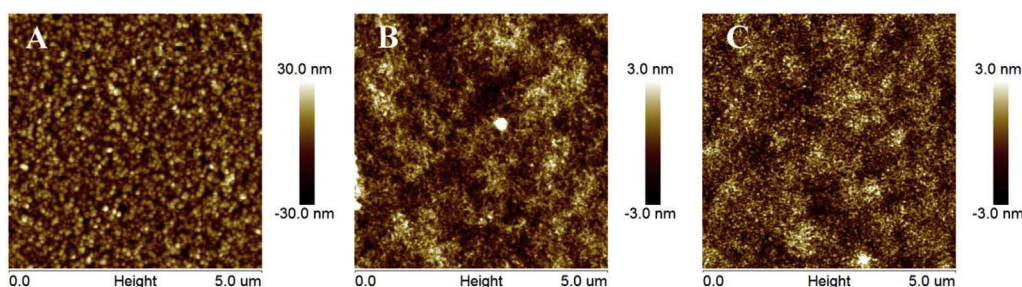
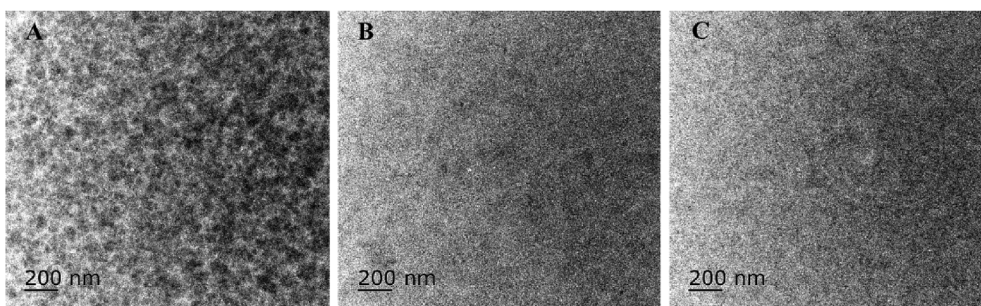
The morphology of the blend films were further studied by transmission electron microscopy (TEM). The relevant images are shown in Fig. 7. Consistent with the large RMS roughness observed in AFM images, the film of PTB7-Th:Tr(Hex)₆-3IC demonstrates obvious phase separation. It is well recognized that excessive phase separation is harmful to efficient exciton dissociation and charge transport. On the contrary, the blend films of Tr(Dec)₆-3IC and Tr(Hex)₆-3BR show homogeneous morphology lacking noteworthy phase separation, agreeing well with the AFM images. Combined, the low electron mobility, the recombination, and the unfavorable morphology explain the low performance of truxene-based solar cells.

4. Conclusion

In summary, three truxene-based acceptors with an aim of extending dimensionality were synthesized for application in OSCs. The

Table 2Photovoltaic parameters of OSCs based on PTB7-Th and truxene-based acceptors under AM 1.5G illumination at 100 mW cm^{-2} .

Acceptor	V_{oc} (V)	J_{sc} (mA cm^{-2})	J_{cal}^a (mA cm^{-2})	FF (%)	PCE (%)	PCE _{max} (%)
Tr(Hex) ₆ -3IC	0.88 ± 0.01	3.71 ± 0.08	3.68	38.1 ± 0.5	1.23 ± 0.05	1.28
Tr(Dec) ₆ -3IC	0.74 ± 0.01	2.55 ± 0.10	2.50	27.9 ± 0.2	0.53 ± 0.02	0.55
Tr(Hex) ₆ -3BR	1.02 ± 0.01	5.92 ± 0.12	5.85	33.4 ± 0.3	2.01 ± 0.09	2.10

^a Calculated from EQE integrations.**Fig. 5.** $J^{1/2}$ - V characteristics of the blend films of PTB7-Th:truxene-based acceptor in (A) hole-only devices and (B) electron-only devices.**Fig. 6.** AFM topographic images ($5 \mu\text{m} \times 5 \mu\text{m}$) of the blend films of PTB7-Th:truxene-based acceptor: (A) PTB7-Th:Tr(Hex)₆-3IC, (B) PTB7-Th:Tr(Dec)₆-3IC, and (C) PTB7-Th:Tr(Hex)₆-3BR.**Fig. 7.** TEM images of the blend films of PTB7-Th:truxene-based acceptor: (A) PTB7-Th:Tr(Hex)₆-3IC, (B) PTB7-Th:Tr(Dec)₆-3IC, and (C) PTB7-Th:Tr(Hex)₆-3BR.

new acceptors differ in the length of side chain (hexyl vs. decyl), π -bridge (thiophene vs. benzothiadiazole), and terminal acceptor unit ((2-(3-oxo-2,3-dihydroinden-1-ylidene)malononitrile vs. 3-ethylrhodanine). The acceptors were evaluated in terms of thermal properties, optical properties, energy levels, and device performance in solar cells. The photovoltaic properties of the truxene-based acceptors were studied by combining with a narrow band-gap donor PTB7-Th. All these three acceptors afforded moderate photovoltaic performance. The reasons were revealed to be low electron mobility, imbalanced transport of hole and electron, serious charge recombination, and unfavorable morphology in blends, which consequently led to low FF and J_{sc} . Nevertheless, this is just a small step on exploiting the potential of truxene-based molecules for use as non-fullerene acceptors in organic solar cells. New molecules with rational design based on truxene are in progress in our lab, which are expected to achieve higher photovoltaic properties in the near future.

Acknowledgments

The research was financially supported by the Startup Fund for Distinguished Scholars of South China University of Technology. This work was also supported by the Ministry of Science and Technology (No. 2014CB643501), the Natural Science Foundation of China (Nos. 21520102006 and 91633301) and the Foundation of Guangzhou Science and Technology Project (201707020019).

Appendix A. Supplementary data

Supplementary data related to this article can be found at <http://dx.doi.org/10.1016/j.orgel.2017.10.009>.

References

- [1] H. Zhou, Y. Zhang, C. Mai, S.D. Collins, G.C. Bazan, T. Nguyen, A.J. Heeger, *Adv. Mater.* 27 (2015) 1767–1773.

- [2] L. Zuo, C. Chang, C. Chueh, S. Zhang, H. Li, A.K.Y. Jen, H. Chen, *Energy Environ. Sci.* 8 (2015) 1712–1718.
- [3] Y. Lin, X. Zhan, *Acc. Chem. Res.* 49 (2016) 175–183.
- [4] Y. Lin, X. Zhan, *Mater. Horiz.* 1 (2014) 470–488.
- [5] S. Holliday, R. Ashraf, C. Nielsen, M. Kirkus, J. Rohr, C. Tan, E. Collado-Fregoso, A. Knall, J. Durrant, J. Nelson, I. McCulloch, *J. Am. Chem. Soc.* 137 (2015) 898–904.
- [6] Y. Lin, J. Wang, Z. Zhang, H. Bai, Y. Li, D. Zhu, X. Zhan, *Adv. Mater.* 27 (2015) 1170–1174.
- [7] J. Jia, N. Zheng, Z. Wang, Y. Huang, C. Duan, F. Huang, Y. Cao, *Sci. China Chem.* (2017), <http://dx.doi.org/10.1007/s11426-017-9102-1>.
- [8] W. Chen, Q. Zhang, *J. Mater. Chem. C* 5 (2017) 1275–1302.
- [9] F. Zhao, S. Dai, Y. Wu, Q. Zhang, J. Wang, L. Jiang, Q. Ling, Z. Wei, W. Ma, W. You, C. Wang, X. Zhan, *Adv. Mater.* 29 (2017) 1700144.
- [10] W. Zhao, S. Li, S. Zhang, X. Liu, J. Hou, *Adv. Mater.* 29 (2017) 1604059.
- [11] W. Zhao, S. Li, H. Yao, S. Zhang, Y. Zhang, B. Yang, J. Hou, *J. Am. Chem. Soc.* 139 (2017) 7148–7151.
- [12] Y. Cui, H. Yao, B. Gao, Y. Qin, S. Zhang, B. Yang, C. He, B. Xu, J. Hou, *J. Am. Chem. Soc.* 139 (2017) 7302–7309.
- [13] Y. Liu, Z. Zhang, S. Feng, M. Li, L. Wu, R. Hou, X. Xu, X. Chen, Z. Bo, *J. Am. Chem. Soc.* 139 (2017) 3356–3359.
- [14] S. Holliday, R. Ashraf, A. Wadsworth, D. Baran, S. Yousaf, C. Nielsen, C. Tan, S. Dimitrov, Z. Shang, N. Gasparini, M. Alamoudi, F. Laquai, C. Brabec, A. Salleo, J. Durrant, I. McCulloch, *Nat. Commun.* 7 (2016) 11585.
- [15] H. Cha, J. Wu, A. Wadsworth, J. Nagitta, S. Limbu, S. Pont, Z. Li, J. Searle, M. Wyatt, D. Baran, J. Kim, I. McCulloch, *J. Durrant, Adv. Mater.* 29 (2017) 1701156.
- [16] D. Baran, R. Ashraf, D. Hanifi, M. Abdelsamie, N. Gasparini, J. Röhr, S. Holliday, A. Wadsworth, S. Lockett, M. Neophytou, C. Emmott, J. Nelson, C. Brabec, A. Amassian, A. Salleo, T. Kirchartz, J. Durrant, I. McCulloch, *Nat. Mater.* 16 (2017) 363–370.
- [17] Y. Lin, P. Cheng, Y. Li, X. Zhan, *Chem. Commun.* 48 (2012) 4773–4775.
- [18] F. Goubard, F. Dumur, *RSC Adv.* 5 (2015) 3521–3551.
- [19] Z. Lu, C. Li, T. Fang, G. Li, Z. Bo, *J. Mater. Chem. A* 1 (2013) 7657–7665.
- [20] H. Zhang, D. Wu, S. Liu, J. Yin, *Curr. Org. Chem.* 16 (2012) 2124–2158.
- [21] Y. Lin, Y. Wang, J. Wang, J. Hou, Y. Li, D. Zhu, X. Zhan, *Adv. Mater.* 26 (2014) 5137–5142.
- [22] X. Zong, M. Liang, C. Fan, K. Tang, G. Li, Z. Sun, S. Xue, *J. Phys. Chem. C* 116 (2012) 11241–11250.
- [23] C. Huang, W. Fu, C. Li, Z. Zhang, W. Qiu, M. Shi, P. Heremans, A.K.Y. Jen, H. Chen, *J. Am. Chem. Soc.* 138 (2016) 2528–2531.
- [24] L. Lin, Y. Tu, C. Tang, Y. Ma, S. Chen, Z. Yin, J. Wei, Q. Zheng, *Chin. J. Struct. Chem.* 35 (2016) 1517–1524.
- [25] T. Lin, B. Tsai, T. Huang, W. Chien, Y. Liu, M. Li, M. Tsai, *Dyes Pigments* 120 (2015) 99–111.
- [26] M. Tehfe, F. Dumur, E. Contal, B. Graff, D. Gigmes, J. Fouassier, J. Lalevée, *Macromol. Chem. Phys.* 214 (2013) 2189–2201.
- [27] J. Luo, Y. Zhou, Z. Niu, Q. Zhou, Y. Ma, J. Pei, *J. Am. Chem. Soc.* 129 (2007) 11314–11315.
- [28] J. Pei, J. Wang, X. Cao, X. Zhou, W. Zhang, *J. Am. Chem. Soc.* 125 (2003) 9944–9945.
- [29] X. Yang, Q. Zheng, C. Tang, D. Cai, S. Chen, Y. Ma, *Dyes Pigments* 99 (2013) 366–373.
- [30] J. Luo, T. Lei, L. Wang, Y. Ma, Y. Cao, J. Wang, J. Pei, *J. Am. Chem. Soc.* 131 (2009) 2076–2077.
- [31] J. Wang, Z. Tang, Q. Xiao, Y. Ma, J. Pei, *Org. Lett.* 11 (2009) 863–866.
- [32] C. Wang, Y. Qin, Y. Sun, Y. Guan, W. Xu, D. Zhu, *ACS Appl. Mater. Interfaces* 7 (2015) 15978–15987.
- [33] K. Balakrishnan, A. Datar, T. Naddo, J. Huang, R. Oitker, M. Yen, J. Zhao, L. Zang, *J. Am. Chem. Soc.* 128 (2006) 7390–7398.
- [34] Z. Tang, T. Lei, J. Wang, Y. Ma, J. Pei, *J. Org. Chem.* 75 (2010) 3644–3655.
- [35] T. Lei, C. Cheng, Z. Guo, C. Zheng, Y. Zhou, D. Liang, J. Pei, *J. Mater. Chem.* 22 (2012) 4306–4311.
- [36] Y. Li, Y. Cao, J. Gao, D. Wang, G. Yu, A.J. Heeger, *Synth. Met.* 99 (1999) 243–248.
- [37] J. Mikroyannidis, P. Suresh, G. Sharma, *Synth. Met.* 160 (2010) 932–938.
- [38] Y. Wu, H. Bai, Z. Wang, P. Cheng, S. Zhu, Y. Wang, W. Mac, X. Zhan, *Energy Environ. Sci.* 8 (2015) 3215–3221.
- [39] S. Chiu, L. Lin, H. Lin, Y. Chen, Z. Huang, Y. Lin, F. Lin, Y. Liu, K. Wong, *Chem. Commun.* 48 (2012) 1857–1859.
- [40] L. Lin, C. Tsai, F. Lin, T. Huang, S. Chou, C. Wu, K. Wong, *Tetrahedron* 68 (2012) 7509–7516.
- [41] M. Scharber, D. Mühlbacher, M. Koppe, P. Denk, C. Waldauf, A.J. Heeger, C. Brabec, *Adv. Mater.* 18 (2006) 789–794.
- [42] S. Dai, F. Zhao, Q. Zhang, T. Lau, T. Li, K. Liu, Q. Ling, C. Wang, X. Lu, W. You, X. Zhan, *J. Am. Chem. Soc.* 139 (2017) 1336–1343.
- [43] Y. Lin, Q. He, F. Zhao, L. Huo, J. Mai, X. Lu, C. Su, T. Li, J. Wang, J. Zhu, Y. Sun, C. Wang, X. Zhan, *J. Am. Chem. Soc.* 138 (2016) 2973–2976.
- [44] Y. Lin, F. Zhao, Q. He, L. Huo, Y. Wu, T. Parker, W. Ma, Y. Sun, C. Wang, D. Zhu, A.J. Heeger, S.R. Marder, X. Zhan, *J. Am. Chem. Soc.* 138 (2016) 4955–4961.
- [45] X. Liu, T. Liu, C. Duan, J. Wang, S. Pang, W. Xiong, Y. Sun, F. Huang, Y. Cao, *J. Mater. Chem. A* 5 (2017) 1713–1723.
- [46] J. Huang, J.H. Carpenter, C.Z. Li, J.S. Yu, H. Ade, A.K.Y. Jen, *Adv. Mater.* 28 (2016) 967–974.
- [47] C. Duan, G. Zango, M.G. Iglesias, F.J.M. Colberts, M.M. Wienk, M.V. Martínez-Díaz, R.J. Janssen, T. Torres, *Angew. Chem. Int. Ed.* 56 (2017) 148–152.
- [48] C. Duan, C. Wang, S. Liu, F. Huang, C.H.W. Choy, Y. Cao, *Sci. China Chem.* 4 (2011) 685–694.
- [49] Z. Wu, Y. Zhu, W. Li, Y. Huang, J. Chen, C. Duan, F. Huang, Y. Cao, *Sci. China Chem.* 12 (2016) 1583–1592.